

## Technical Features of a CCD Video Camera System to Record Cardiac Fluorescence Data

WILLIAM T. BAXTER,\* JORGE M. DAVIDENKO,\* LESLIE M. LOEW,† JOSEPH P. WUSKELL,† and JOSÉ JALIFE\*

\*Department of Pharmacology, SUNY Health Science Center at Syracuse, Syracuse, NY, and †Department of Physiology, the University of Connecticut Health Center, Farmington, CT

**Abstract**—A charge-coupled device (CCD) camera was used to acquire movies of transmembrane activity from thin slices of sheep ventricular epicardial muscle stained with a voltage-sensitive dye. Compared with photodiodes, CCDs have high spatial resolution, but low temporal resolution. Spatial resolution in our system ranged from 0.04 to 0.14 mm/pixel; the acquisition rate was 60, 120, or 240 frames/sec. Propagating waves were readily visualized after subtraction of a background image. The optical signal had an amplitude of 1 to 6 gray levels, with signal-to-noise ratios between 1.5 and 4.4. Because CCD cameras integrate light over the frame interval, moving objects, including propagating waves, are blurred in the resulting movies. A computer model of such an integrating imaging system was developed to study the effects of blur, noise, filtering, and quantization on the ability to measure conduction velocity and action potential duration (APD). The model indicated that blurring, filtering, and quantization do not affect the ability to localize wave fronts in the optical data (*i.e.*, no systematic error in determining spatial position), but noise does increase the uncertainty of the measurements. The model also showed that the low frame rates of the CCD camera introduced a systematic error in the calculation of APD: for cutoff levels >50%, the APD was erroneously long. Both noise and quantization increased the uncertainty in the APD measurements. The optical measures of conduction velocity were not significantly different from those measured simultaneously with microelectrodes. Optical APDs, however, were longer than the electrically recorded APDs. This APD error could be reduced by using the 50% cutoff level and the fastest frame rate possible.

**Keywords**—Optical mapping, Voltage-sensitive dyes, Electrophysiology, Conduction velocity, Action potential duration.

*Acknowledgment*—Thanks to Arkady Pertsov and Candido Cabo for helpful discussions; John Kauer and Gino Cinelli for assistance in developing the video optical mapping system; Joanne Getchonis, Wanda Coombs, Christine Kapuscinski, and Jiang Jiang for technical assistance; and LaVerne Gilbert for secretarial help. This study was supported by Grants PO1-HL39707, RO1-HL29439, and RO1-GM35063 from the National Heart, Lung, and Blood Institute; the National Institutes of Health; and the National Institute of General Medical Sciences. Jorge M. Davidenko is an Established Investigator of the American Heart Association.

Address correspondence to William T. Baxter, Department of Pharmacology, SUNY Health Science Center, 766 Irving Avenue, Syracuse, NY 13210, U.S.A.

(Received 30Aug95, Revised 8Mar96, Revised 15July96, Accepted 17Oct96)

### INTRODUCTION

Greater understanding of cardiac arrhythmias has increased the demands for more sophisticated tools to describe the activation and recovery processes of the heart. Propagation abnormalities in the heart, including reentrant excitation, may occur over various spatial scales, ranging from so-called micro-reentrant loops to rotors giving rise to spiral waves that encompass the entire ventricle (5,12,14). Therefore, it is desirable that a mapping system should cover a relatively large area with closely placed recording sites. Toward this aim, multiple extracellular electrodes have been used in many laboratories to map the electrical activity from subepicardial, subendocardial, and intramural regions of the heart (8,12). Optical mapping via voltage-sensitive dyes, developed by Cohen and his colleagues (4,10), has been used to monitor the electrical activity of excitable cells in nervous tissue, skeletal muscle, and cardiac muscle (15,27). In 1976, Salama and Morad (28) made the first optical recordings of cardiac action potentials. Multiple site optical mapping in the heart has been achieved using arrays of photodiodes or laser scanning (7,9,13). Because the number of photodetectors may be increased without incurring increased injury to the tissue, optical methods provide a unique opportunity to take high-resolution movies of electrical activity in excitable tissues.

Charge-coupled device (CCD) cameras have been successfully used as photodetectors with voltage-sensitive dyes (2,18) and other fluorescent probes (19), but they have not found widespread use in cardiac optical mapping due to their slow frame rates. Whereas photodiodes continuously generate current in response to light flux in a manner analogous to electronic recording systems, each frame of a CCD movie integrates light over a discrete interval in a manner analogous to a photographic process. CCD elements, here called pixels, generate charge as they collect light over an interval. The accumulated charge is then shifted off the CCD chip pixel by pixel and converted to a video signal comprised of voltages. One collection

interval corresponds to a single picture, or frame, in the resulting movie. Each frame represents light collected simultaneously by all pixels over the same interval. The pixels are then reset to zero charge, and the collection phase is started again for the succeeding frame.

CCD cameras fall roughly into two categories: scientific grade and video rate cameras. Scientific, cooled CCDs have low noise, large dynamic range and frame readout rates on the order of seconds or even minutes (17). Video CCD cameras, using special circuitry for rapid data readout, operate in the U.S. at the standard television rate of 30 frames/sec. Currently, the most common architecture for video cameras is the frame transfer CCD, which has a second array masked from light for storing image data (22). At the end of the light collection interval, the image is rapidly moved (within microseconds) from the primary accumulation array to the storage array. Readout then occurs from the storage array during the next frame period of the primary array. Compared with their high-performance counterparts, video CCDs suffer from reduced signal-to-noise ratios (SNRs) and smaller dynamic range. Comparing these three sensor technologies, photodiodes have good SNRs, fast readout, but low numbers of recording elements. Scientific cameras have good SNRs, a large number of elements, but slow rates of readout. Video CCDs have low SNRs, but possess a large number of elements and readout that is fast enough for some applications. Therefore, video CCD cameras currently provide the best opportunity for taking high-resolution optical movies of cardiac activity.

We have configured a video CCD camera in our laboratory to acquire data at rates up to 240 frames/sec, providing a system for high-resolution optical mapping in the heart. In this paper, we describe the imaging process in a discrete integrating system, the advantages and the limitations of this system in the study of propagating waves in two-dimensional preparations of cardiac tissue, the calculation of conduction velocity (CV) and action potential duration (APD) from the optical data, and their comparison with microelectrode recordings. A computer model of the imaging process was developed to understand better the individual effects of noise, sampling, and blur on the recorded data. Studies of arrhythmias with the video system have been published elsewhere (1,5,14,23); here, we seek to establish a quantitative understanding of the relationship between the video optical signal and the electrophysiological parameters in ventricular epicardial muscle preparations.

The following definitions and conventions will be used:

*Pixel*: a spatial unit of measure in digitized images representing both an individual photoelement and its corresponding point in the acquired image data.

*Frame*: a single picture in a movie sequence; also used as a temporal unit of measure.

*t* (msec/frame): the integration period or frame interval, during which the photosensitive elements collect light.

*1/t*: the temporal sampling frequency, also called the *frame rate* (Hz).

*x* (mm/pixel): the spatial sampling interval; the diameter of the area projected onto a single pixel.

*1/x*: the spatial sampling frequency (*i.e.*, the resolution in pixels/mm).

## METHODS

### *The Preparation and Recording*

Details of the tissue preparation, staining technique, and chamber have been described elsewhere (3,5,23). Briefly, square sheets of sheep ventricular epicardial muscle ( $20 \times 20 \times 0.5$  mm) were pinned to the floor of a superfusion chamber containing Tyrode's solution. Long Ag/AgCl electrodes embedded in the floor of the chamber could produce planar waves from any side of the preparation. To avoid mechanical artifacts, the electromechanical uncoupler diacetyl monoxime (10 to 15 mM) was added to the superfusate before recording (20). In addition to optical recordings, transmembrane potentials were monitored using glass microelectrodes filled with 3 M KCl connected to an amplifier (WPI, Sarasota, FL, USA). After 1 hr of tissue equilibration, superfusion was halted, and the voltage-sensitive dye di-4-ANEPPS (5  $\mu$ g/ml) was added to the chamber. Di-4-ANEPPS is a soluble styryl fluorescent indicator of transmembrane potential, with good sensitivity, long bleaching time, and a response time of a few microseconds (21).

For measurements of CV, the fiber orientation was first determined optically by stimulating the center of the tissue with a concentric bipolar electrode (1.6 mm diameter) and observing the orientation of the elliptical wave. Two glass microelectrodes were placed at opposite ends of the preparation (1.5 to 2 cm apart) for longitudinal recordings at various cycle lengths, then at the perpendicular sides for transverse recordings. Recordings were made simultaneously from the video camera and both electrodes. Velocity measurements from optical data were determined from isochrone maps (see below). Optical recordings were compared with electrode recordings by a Wilcoxon matched pairs test.

### *Optics and Camera*

Light from a 250 W tungsten-halogen lamp (Osram, Chicago, IL, USA) passed through a collimator, a heat filter, a bandpass excitation filter (530 nm,  $\pm 30$  nm), a defocusing lens, and was reflected by a dichroic mirror (580 nm) onto the preparation, thus creating a uniform circular field of illumination (2.3 cm diameter,  $5 \times 10^4$  lux). To minimize bleaching of the dye, the tissue was

only illuminated during data acquisition. Fluorescence from the tissue was transmitted through an emission filter (640 nm,  $\pm 50$  nm) to a CCD video camera (Model 6510, Cohu, Inc., San Diego, CA, USA), with the following specifications:  $739 \times 480$  CCD elements ( $8.5 \times 9.8$   $\mu\text{m}$  each) in a  $6.4 \times 4.8$  mm array; SNR = 56 dB; sensitivity = 0.4 lux; quantum efficiency = 40 to 60% in the range of the emission filter; and external controls for gain and video offset (black level). All experiments were conducted with the automatic gain control turned off. A TV zoom lens ( $f = 12.5$  to 75 mm, F/1.8, Javelin) attached to the camera focused the image onto the CCD array. The working distance between the lens and the preparation was 16 cm. The numerical aperture of this lens (0.28) was comparable with those obtained in tandem-lens macroscopic systems (24), whereas the zoom function provided a simple way to change magnification.

Camera output was digitized at 8 bits/pixel (256 gray levels) by the A/D converter of a frame grabber board (Model 12, Epix, Inc., Buffalo Grove IL, USA), written to the board's 16 megabytes (Mb) of video memory, then stored to the hard disk of an IBM-compatible personal computer. Viewed on the display monitor, the gray level brightnesses representing fluorescence intensity varied across the surface of the preparation, due to spatial variations in staining. Because the voltage-dependent optical signal was a small decrease in fluorescence superimposed on this background, the signal was maximized by stretching the contrast of the image to fill all 256 gray levels. Gain and black level were adjusted until the darkest areas of the tissue appeared nearly black and the brightest areas were nearly white (saturated). For comparisons of SNRs at different magnifications and frame rates (see *Results*), the camera settings were not optimized, but kept fixed at intermediate settings.

To visualize the spatial organization of propagating waves, a background image of quiescent tissue was subtracted from each frame of the movie. The background image was either a single frame acquired just before taking the movie or else the average of several frames from the diastolic intervals of the movie. Background fluorescence decreased slowly over several hours, but remained stable during a single acquisition (lasting seconds at most), as seen by flat, stable baselines.

#### *Temporal and Spatial Sampling*

The 30-Hz temporal sampling rate was doubled to 60 Hz (16.7 msec interframe interval) by using noninterlaced video, which ignores alternate lines, reducing the maximum number of lines from 480 to 240 usable lines of video. Thus, the vertical spatial resolution was always half the horizontal resolution for all movies acquired with this system. For display, each line was displayed twice to

maintain the correct aspect ratio. Even faster rates were obtained using external reset (modification ER-4318, provided by Cohu). In standard video, sensor integration is halted, and frame readout is initiated by a vertical reset signal every 16.7 msec. This process may be speeded up by sending the vertical reset at a faster rate, before the entire frame is read out, decreasing the number of usable video lines. For example, if the reset signal is sent at twice the usual rate, frames will integrate over 8.3 msec intervals, cutting the light collection time in half, and only the top half of the frame will be read out. The Epix frame grabber board was programmed to provide the external vertical reset signal at 240, 120, and 60 Hz providing frame intervals of  $t = 4.2, 8.3,$  and 16.7 msec, with 60, 120, and 240 usable horizontal lines of video, respectively.

Magnification was adjusted with the zoom lens of the camera. In the horizontal direction, the spatial resolution ( $x$ , the interpixel spacing) ranged from 0.14 mm to 0.036 mm. In imaging a 2-cm-wide field, this resulted in pictures ranging from 143 to 556 pixels in diameter. The frame grabber could treat any subset of the usable array as the current field of view. The maximum duration of a single acquisition was a function of the sampling rate, image size, and available frame grabber memory (*e.g.*, for a  $300 \times 120$  pixel image acquired at 120 Hz, the frame grabber's 16 Mb of memory could acquire a sequence of 3.9 sec duration. About 12 sec were required to write the data to the computer's hard drive before another movie could be acquired.

#### *The Imaging Process and Data Analysis*

Because CCD cameras integrate light collection over time and space, moving objects are blurred in the resulting movie data. The amount of blur  $s$  is a function of object velocity and temporal and spatial sampling:  $s = vt/x$ , where  $s$  is blur in pixels/frame,  $v$  is velocity in mm/ms, and  $x$  and  $t$  are the spatial and temporal sampling intervals. In particular, the front of a moving wave with a square step edge would be recorded as a ramp, as shown in Fig. 1A. The location of the square wave may be determined from the ramp profile: the wave front was at the top of the ramp (position a in Fig. 1) at the beginning of frame integration, and at the bottom of the ramp (position b in Fig. 1) at the end of frame integration. In the next frame, the top of the ramp will be at the same position as the bottom of the ramp in the previous frame.

Figure 1B depicts how the data appear in the temporal dimension (*i.e.*, multiple frames make up a single pixel's value over time). In a discrete integrating system, the "up-stroke" will always take two frames to reach the maximum. For the frame interval illustrated in Fig. 1A, pixels to the left of position b will finish integrating before the wave, and therefore any light, arrives at their position. They will output zero for this frame. Pixels to the right of

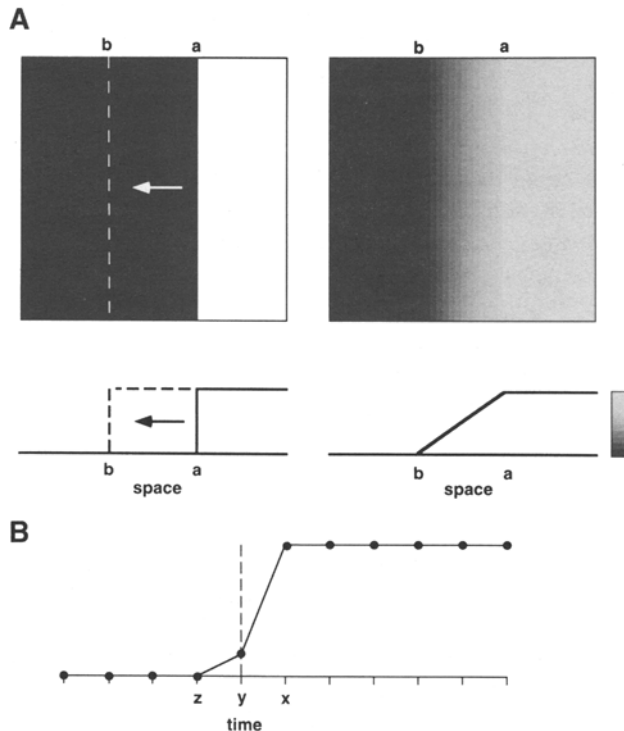


**FIGURE 1.** (A) A moving object (left) is blurred during integration (right) of a single frame. (Left) A white bar moves from left to right during 1 frame interval starting at *a*. By the end of the frame, the edge will reach the dotted line at *b*. (Right) The single frame acquired by the video system shows a blurred edge. Horizontal cross-sections of pixel gray values are shown below each image. The step edge profile of the white bar becomes a ramp in the blurred image. The top of the ramp at *a* corresponds to the location of the edge at the start of frame integration, whereas the ramp bottom, *b*, reflects the edge location at the end of the integration period. Horizontal axis of profiles corresponds to same axis of images. (B) Values of several frames at a single pixel over time during passage of the white bar. Tic marks represent single frames, values are connected by straight lines. Frame at *y* has intermediate value due to passage of the edge during that frame interval [*i.e.*, this pixel is between *a* and *b* in (A)]. The intermediate value at *y* could be anywhere between the minimum and maximum values (dotted line), depending where it is located between *a* and *b*.

position *a* will record the maximum value of the wave for the entire interval and output the corresponding maximum value. Those pixels between *a* and *b* will record the maximum wave amplitude, but only for some fraction of the frame interval, and will output an intermediate value. This intermediate value may be anywhere between zero and the maximum, depending where the pixel occurs on the ramp. Note that, although the wave front is blurred in the integrated data, the position may be exactly determined at the start and end of each frame interval (and hence at intermediate times if constant velocity is assumed).

**Isochrones for CV.** The following algorithm was used for generating isochrone lines from the image data. Scan-

ning each pixel's values over time, a frame was labeled as a wave front if its value was greater than the previous frame's value, and if this difference was greater than a threshold [*i.e.*, label  $p_i$  as a wave front if  $p_i - p_{i-1} > \frac{1}{2}(\max - \min)$ ], where  $p_n$  is the value at frame  $n$ ,  $\max$  is the maximum value during the action potential, and  $\min$  is the average of several baseline frames immediately before and after the action potential. Using this criterion, frame  $x$  in Fig. 1B would be labeled but not frame  $y$ . Because of propagation-induced spatial blurring, a set of pixels perpendicular to the wave front would be labeled in a single frame, resulting in isochrone "bands" with width equal to the amount of blur. The centers of these bands correspond to the tops and bottoms of the ramps. When bands from several frames are displayed together, the boundaries between the bands fall on the centers of the ramps and thus provide a good estimate of the location of the wave at the middle of the frame interval (see inset of Fig. 5). These boundaries were used as isochrone "lines" (see Fig. 6).

Pixel distances were always calibrated with an image of a scale bar. Local conduction velocity,  $v$  (in mm/msec), was calculated between two isochrone lines  $i$  and  $i+n$  as  $v = d/nt$ , where  $n$  was the number of intervening isochrone lines,  $t$  the frame interval in msec, and  $d$  the distance in mm between the isochrone lines, perpendicular to  $i$ 's tangent at the point of measurement.

**APD.** The APD was measured, after filtering, from the upstroke to the point in time when the fluorescence returned to a given proportion (50, 70, or 90%) of the resting value, called the cutoff level. Each pixel's values over time were scanned until the values reached the cutoff level, determined from the computed baseline and signal levels. To counter the effects of noise, the values were scanned in both the forward and reverse directions. Two points were chosen to guide the search for the cutoff level in the wave front:  $\max$ , the maximum value of the action potential, and  $b$ , a point on the baseline before the action potential. Points were scanned from  $b$  toward  $\max$  until the cutoff level was reached; this point in time was labeled  $c1$ . Then points were scanned in reverse from  $\max$  toward  $b$  until the cutoff was again encountered, and labeled  $c2$ . The average of  $c1$  and  $c2$  was considered the actual cutoff point. The same strategy was used in the repolarizing tail with  $\max$  and  $b$ ; this time, the latter was a point on the baseline after the action potential.

**Filtering.** Before generating isochrone lines or measuring APD, a low-pass spatial filter was applied to each frame by convolution with two-dimensional circularly symmetric Gaussian kernels (26), which set each pixel to the weighted average of its neighbors. The size of the neighborhood was determined by  $\sigma$ , the standard deviation of the Gaussian, with larger  $\sigma$  filtering out more of the high

spatial frequencies. Filters were evaluated by their effects on the SNRs of the data over time. The SNR for a movie was calculated over time for each pixel, and the results were averaged. SNR was computed as  $S/N_{RMS}$ , where  $S$  is the mean number of peak gray levels for the set of activations in a given trial, and  $N_{RMS}$  is the root mean square of the baseline during periods between activations. After filtering, the gray level contrast was stretched to fill all 256 levels, by rescaling the data so that the maximum pixel value from the movie was 255 and the movie's minimum value was 0.

#### Model of Image Blur

A computer model was developed to study the effects of blur, noise, and quantization on propagating waves, and to evaluate the correlation between video optical mapping and microelectrode recordings. For CV measures, movies of a moving white bar (step edge profile) were generated to study effects of noise and sampling. Electrode recordings of real action potentials were digitized and converted to video movies of planar waves to study accuracy of APD measurement. The temporal sampling rate of these artificially generated movies could be decreased to observe the effects of low frame rates on the shape of action potentials. Specifically, microelectrode action potentials from sheep epicardial muscle were recorded on a digital storage oscilloscope (Model 2214, Tektronix, Beaverton, OR, USA) and written to a personal computer with the oscilloscope's accompanying Grabber software (0.25 msec sampling). These time series were resampled to create a function over time,  $h(z)$ , with 1 msec/frame sampling. Movies  $M(x, y, z)$ , where the indices correspond to the horizontal, vertical, and time axes respectively, were generated using  $M(x, y, z + x) = h(z)$ . This created a movie of a planar wave moving from left to right, with the wave front propagating 1 pixel/frame, termed the nonblur condition. Blur could be introduced and the results compared with the nonblurred movie by decreasing the model's frame rate. Each frame of movie  $M$  was blurred by taking the spatial waveform of each line  $f(x)$  and shifting its  $s$  pixels. The blurred spatial waveform  $g(x)$  was computed for each line as:

$$g(x) = 1/s \sum_{j=0}^{s-1} f(x+j). \quad (1)$$

The effect of this algorithm is to convert a step edge into a ramp (Fig. 1A), with ramp width =  $s$ . The standard movie (*i.e.*, highest frame rate) consisted of either a white bar or an action potential, propagating at 0.1 mm/msec, with spatial sampling  $x = 0.1$  mm/pixel and temporal sampling  $t = 1$  msec/frame. APD was 200 msec at the 70% level, amplitude was 256 gray levels, and noise was 0. For comparisons, either the frame rate was decreased by the above algorithm, or the number of amplitude levels

was reduced for quantization studies, or varying amounts of pseudorandom Gaussian noise with a specified standard deviation were added. This model enabled us to examine the individual contributions of temporal sampling rate, quantization, and noise on distortion of the spatial waveform and measurement error in CV and APD for planar wave front propagation.

## RESULTS

### Characteristics of the Video Optical Signal

Transmembrane electrical activity in the preparation can be observed on the video monitor as a transient decrease in the intensity of emitted light. Data must be digitized and processed, however, before detailed characteristics of the propagating wave may be appreciated. Figure 2 shows three stages in the processing of a single video frame obtained during the propagation of a planar wave from right to left, which was initiated by linear stimulation of the right border of the tissue. Figure 2A shows the image of the preparation before processing. The dark diagonal lines are small arteries, ranging from 0.1 to 0.4 mm in diameter. Several white spots at the center of the preparation are the result of overstaining and excess of fluorescence (*i.e.*, saturation of the camera sensors). The black shadow on the right border is a concentric bipolar electrode, used for extracellular recording. The recording area is  $\sim 15 \times 20$  mm. As a result of the low level of the signal and the nonuniform level of fluorescence, the propagating wave, although visible in real time, is not apparent in the still picture. Figure 2B shows the same frame after subtraction of the background image of the preparation. The right part of the preparation is undergoing activation, displayed as white. The left part of the preparation, displayed as black, is at rest. After subtraction, the optical signal in epicardial preparations ranged from 1 to 6 gray levels (mean  $3.0 \pm SD 1.3$ ). Figure 2C shows the same frame after application of the spatial filter ( $\sigma = 2.5$  pixels) and contrast enhancement. The small arteries undergo no electrical activation and are visible in the right side (*i.e.*, activated region) of Fig. 2B,C as black diagonal lines.

### Spatial Filtering and SNR

Although the optical signal is readily apparent when viewing subtracted images, as in Fig. 2B, the SNR over time is low for a single pixel. Filtering in the spatial domain was applied to improve the SNR of the data in the time domain. In particular, positioning isochrone lines and determining the APD required that individual activations were clearly distinguished over time. Figure 3 shows the time series of a single point subjected to spatial filters of various sizes (Fig. 3A). The frame rate was 4.1 msec. Figure 3B shows a snapshot of the corresponding movie

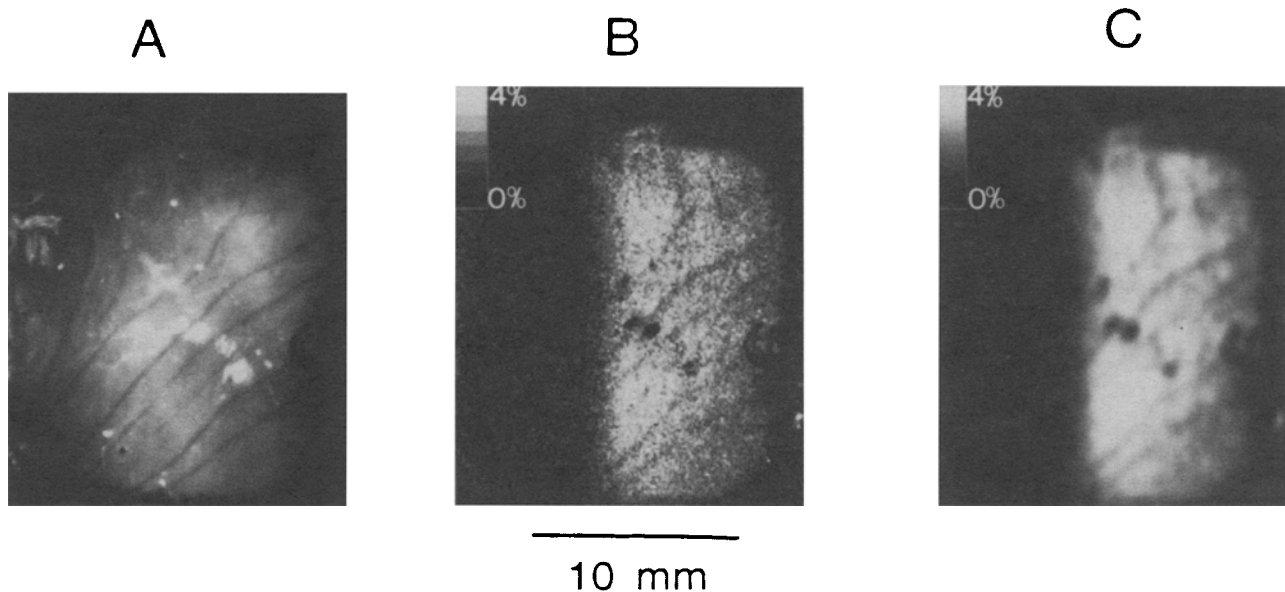


**FIGURE 2.** Cardiac electrical activity seen by the video camera. (A) Image of the preparation after staining with voltage-sensitive dye. (B) One frame from the movie of a planar wave moving right to left. The background image fluorescence has been subtracted, leaving only the electrical activity (white). (C) Same as (B) after applying the spatial filter ( $\sigma = 2.5$  pixels) and contrast stretch. Intensity scale bars in (B) and (C) show 0% and 4%  $\Delta F/F$  as their darkest and brightest values, respectively.

data, and Fig. 3C shows a microelectrode recording simultaneous with Fig. 3A. Optical data were not subjected to contrast stretching after filtering. Although activations are difficult to recognize in the time series of a single point in the unfiltered data (top line of Fig. 3A), when viewed as a movie or even as a single image frame, the wave front is readily apparent (Fig. 3B, top). This is the basis for using spatial filtering: the image data contain information that dramatically improves the SNRs in the temporal dimension. Figure 3A also shows that, as the Gaussian spatial filter increases in size, specified by  $\sigma$  in pixels, the action

potentials become more defined and bear greater resemblance to the microelectrode recording in Fig. 3C, up to a point of diminishing returns. In the spatial domain, the image becomes more blurred with increasing filter size (Fig. 3B). When the spatial filter was large enough to provide a SNR around 10 ( $\sigma = 3$  in Fig. 3A), APDs were consistent within a single recording and changed little with larger filters. The average SNR in the video optical data was  $2.5 \pm 0.8$ ; a filter with  $\sigma = 2.5$  was most commonly used.

As shown in Fig. 4, the SNR decreased as the frame

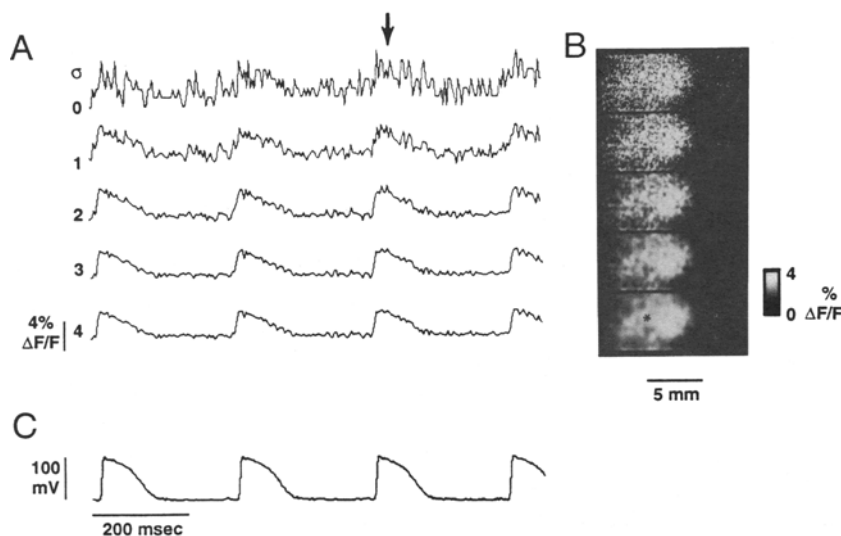


**FIGURE 3.** Optical recording of cardiac activity: effect of the spatial filter. Filter size is specified by  $\sigma$  (in pixels), the standard deviation of the Gaussian convolution kernel.  $\sigma = 0$  indicates no filter. (A) Approximately 1 sec of video data from one pixel, subjected to spatial filters of increasing size. As  $\sigma$  increases, more and more high frequencies are filtered out and action potentials become more defined. Frame rate = 240 Hz. Arrow denotes time of snapshot in (B). (B) Single frames from the movie data show a wave moving left to right. As  $\sigma$  increases, the images are progressively blurred. Asterisk denotes location of optical (A) and electrode (C) recordings. (C) Intracellular microelectrode recording taken simultaneous with (A). Filter size,  $\sigma$ , applies to time plots in (A) and images in (B). Time scale applies to (A) and (C). Contrast was not stretched after filtering, therefore fluorescence scales apply to all traces in (A) and images in (B).

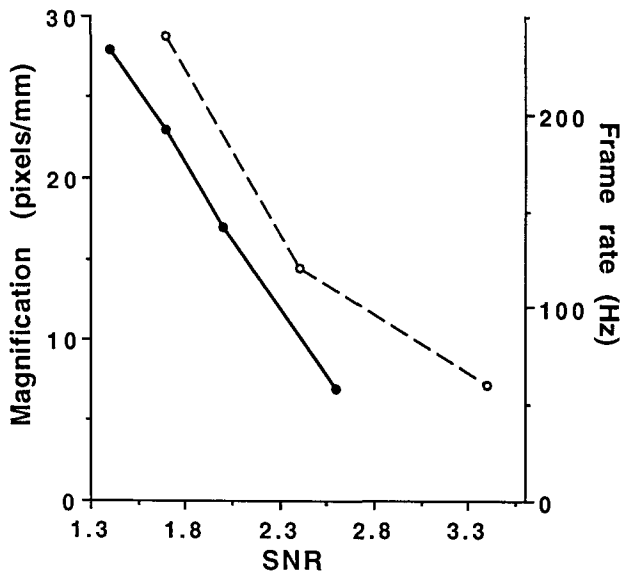


**FIGURE 4.** SNR in the optical recordings. SNR decreased with increases in magnification (solid line) or frame rate (dotted line). Magnification data are all at 8.3 msec frame interval (120 Hz); frame rate data are all at a magnification of 17 pixels/mm.

rate and magnification were increased. Changes in the temporal and spatial sampling rates altered the background light level and amount of signal (both measured in gray levels). As magnification increased (decreasing the inter-pixel distance  $x$ ), individual pixels covered a smaller area of tissue, received fewer incident photons, resulting in reduced brightness in the images and reduced signal. Similarly, as the frame rate was increased (decreasing the interframe interval  $t$ ), pixels integrated light for shorter periods, also causing darker images and reduced signal.

*Isochrones and CV*

**The Imaging Model.** A movie of a white bar with a step edge profile was used for generating isochrone lines and measuring wave velocity in the model. The activation labeling algorithm labeled wave fronts in the standard movie with an accuracy equivalent to the spatial resolution (*i.e.*, 0.1 mm or 1 pixel). When the model's frame rate was reduced, blurring the propagating wave, the step edge profile was changed to a ramp. The set of points labeled as activations in each frame increased from thin lines to thick isochrone bands whose width, in pixels, was equal to the amount of blur. Isochrone lines, defined as the borders between successive bands, fell on the center of the blurred ramps of the propagating waves (Fig. 5, inset).

When the spatial filter was applied to data blurred by low frame rates, the resulting profiles were nearly the same as blurring alone, with some smoothing of the corners of the ramp. Isochrone lines were still located at the center of the ramps. The spatial filter has little effect at low

temporal sampling rates, which, in effect, introduce another form of low-pass filtering.

In the absence of noise, isochrone lines were 1 pixel wide (here width refers to the direction parallel to the direction of propagation). When noise was added to the movies, points labeled as wave fronts were erroneously displaced from the actual position. The isochrone lines dissolved into clouds of points with increasing standard deviation (SD), although the average computed wave front location was still the correct value. As shown in Fig. 5, with increasing noise, the SNRs decreased and the SD of the localization error increased (black symbols). Spatial filtering ( $\sigma = 2.5$ ) dramatically decreased the SD of error (white symbols). Different amplitudes (signal = 1, 5, 10, and 255 gray levels) displayed the same error *versus* SNR curves, indicating that neither the absolute magnitude of the signal nor its quantization are a factor in localization of wave fronts. These simulations used a movie of a drifting white bar with a step edge profile; the same accuracy of wave front localization was obtained for movies of a digitized action potential.

**CCD Data from Optical Mapping Experiments.** The wave front-labeling algorithm (see *Methods*) was applied to a sequence of frames from an optical recording to obtain a set of isochrone bands, which were combined to generate isochrone lines. Figure 6 shows isochrone lines for planar waves propagating in the transverse (Fig. 6A, top) and

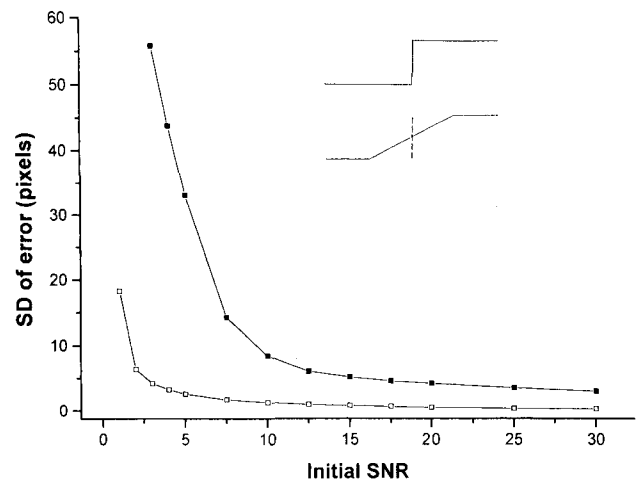


**FIGURE 5.** Computer model: determining wave front location in the presence of noise. Gaussian noise with varying SD was added to an artificial movie to obtain the desired SNR. With no noise, the wave front (upper inset) was located at the center of the blurred ramp in the movie data (lower inset). Error refers to displacement of the computed wave front from the actual position. Decreasing SNR scattered this computed wave front, shown by increasing SD in measurements (black squares). When a Gaussian filter ( $\sigma = 2.5$ ) was applied to noisy movies, the error was greatly diminished (white squares). Initial SNR refers to original SNR before filtering (black squares).

longitudinal (Fig. 6B, top) directions, relative to the myocardial cell orientation. This approach for determining isochrone lines (*i.e.*, the position of the wave front) always assigned the wave front to a point roughly in the center of the blurred waveform's spatial upstroke. The middle of Fig. 6A shows an isochrone line, computed for transverse propagation, superimposed on the corresponding image. The brightness profile at the bottom shows a horizontal line of pixels about three-fourths from the top of the image. The spike in the middle of the spatial upstroke represents the location of the isochrone line. Figure 6B shows similar images for the longitudinal planar wave, with the lower profile showing a vertical line of pixels. The more rapid longitudinal wave has more widely spaced isochrone lines (top), is more blurred (middle), and its upstroke ramp

is less steep (bottom). Average conduction velocities were 0.13 mm/msec for the transverse wave and 0.35 mm/msec for the longitudinal wave, although frame-to-frame variations are detectable in Fig. 6A for the transverse wave.

Isochrone lines were assigned to the same part of the spatial upstroke from frame to frame, allowing CVs to be reliably calculated from the optical data. Figure 7 shows CVs computed from optical data (white symbols) *versus* those measured simultaneously using microelectrodes (black symbols) in a representative experiment at various basic cycle lengths of stimulation. The differences in transverse velocities as measured by the two techniques were within 0.005 mm/msec on average, whereas the average longitudinal difference was 0.023 mm/msec (three preparations). The Wilcoxon test for matched pairs

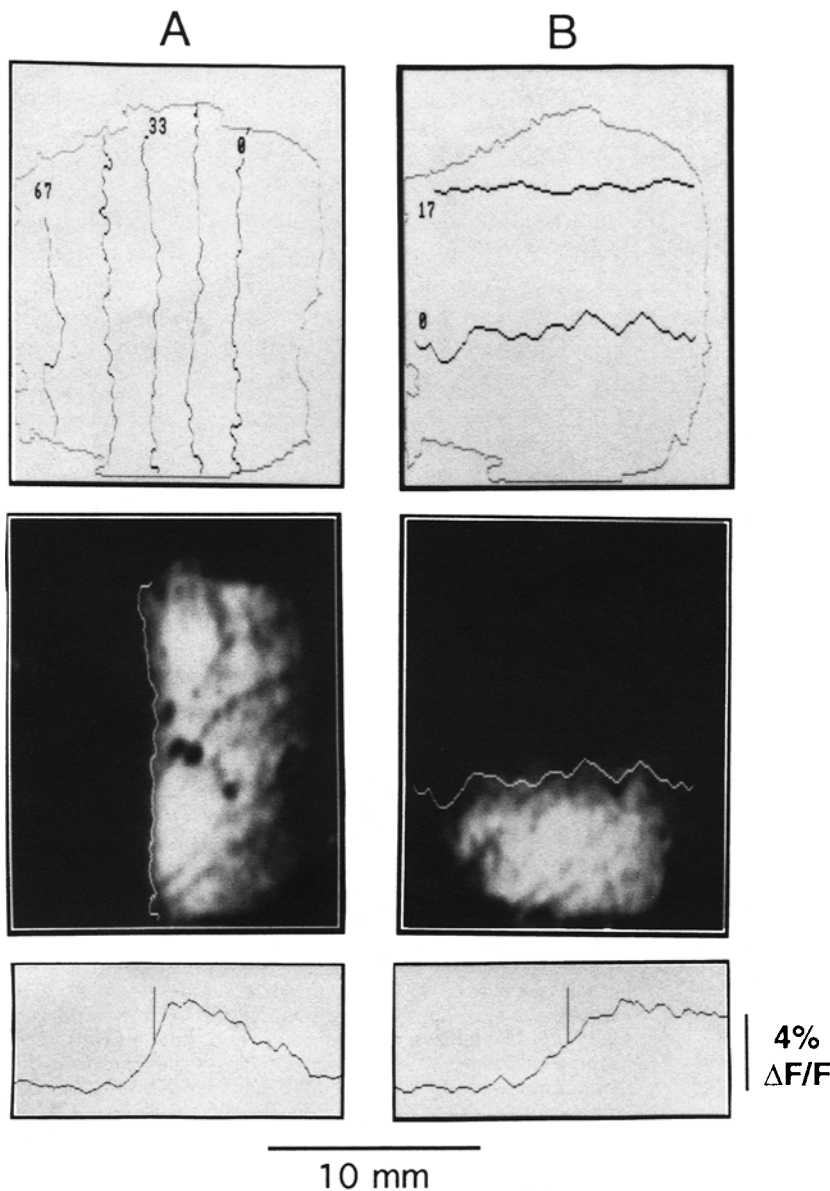


**FIGURE 6.** Isochrones in optical recordings of cardiac activity. (A) Top: isochrone map of planar wave moving right to left. Center: single isochrone from (A) superimposed on the corresponding frame of video data (filtered with  $\sigma = 2.5$ ). Bottom: horizontal line of gray levels from the image frame showing the spatial profile of the activation wave. Spike corresponds to isochrone line. (B) Data from a longitudinal wave in the same preparation. Lower profile shows a vertical column of pixels from the corresponding image (B, center). Scale bar refers to horizontal axis in bottom profiles and both axes in other panels. Frame rate is 60 Hz in both examples.

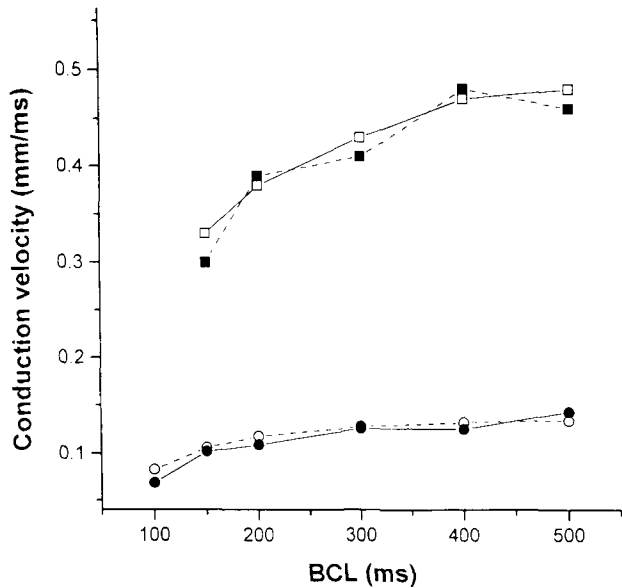


**FIGURE 7. Recordings of cardiac activity. Comparison of CV versus basic cycle length (BCL) measured by electrodes (black symbols) and video data (white symbols), for longitudinal (squares) and transverse (circles) propagation, in one experiment.**

showed no significant difference between optical and electrode measures of conduction velocity ( $p = 0.21$  transverse,  $p = 0.23$  longitudinal).

APD

The APD as measured by the optical system is affected by many factors, including temporal and spatial sampling, the shape of the waveform, noise, filtering, quantization, and the choice of cutoff level. In the model system, the nonblurred standard movie of a digitized action potential was subjected to different temporal sampling rates, spatial filters of different sizes, and varying amounts of noise and amplitude quantization. The APDs from these modified movies were measured by the computer algorithm (see

*Methods*) and compared with the APDs in the nonblurred standard.

The inset of Fig. 8A shows the original standard action potential (top), the 16.7 msec samples at 60 Hz (middle), and the linearly interpolated 16.7 msec samples superimposed on the standard action potential (bottom). These traces show that reduced temporal sampling has several effects on the wave shape over time: the steep upstroke is converted to a ramp (because the algorithm for APD essentially interpolates between samples), the maximum amplitude is slightly decreased, and there are slight quantization effects in the tail. APD error at three cutoff levels for several frame rates is plotted for the computer model (Fig. 8A) and optical data from epicardial preparations (Fig. 8B). APD error in the model is the difference between APDs in the standard (1 msec sampling) and modified (sampling > 1 msec) movies. APD error in the experimental data is the difference between APDs measured by the CCD camera versus microelectrodes at the same position. In both model and experiment, APD error increased with increasing frame interval (decreasing frame rate). Of the three cutoff levels tested, the 50% level had the least error. For cutoff levels >50%, the APD error was always positive (longer APD when  $t > 1$  msec).

What are the effects of the Gaussian spatial filter on APD? The spatial filter blurs in space, but it also affects the duration of the wave over time. In the upper inset of Fig. 9, the time plot of the standard movie goes to its maximum value in 1 frame. Superimposed is the same movie's time series after spatial filtering with a large kernel ( $\sigma = 12$ ), now with a sinusoidal "upstroke" (very large kernels are required to make this effect noticeable). The spatial filter has altered the waveform over time; clearly, the 90% level is more affected than the 50% level. The lower plot of the inset shows the time series of the same movie before and after filtering, but with the frame rate adjusted to induce a blur of 18 pixels. In this case, the effects of the spatial filter are negligible. Therefore the effects of the spatial filter are such that (a) increasing the

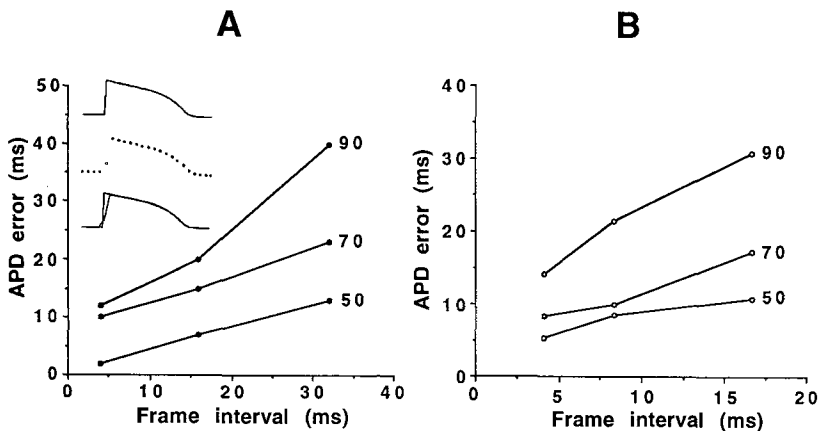


**FIGURE 8. Effects of frame rate on APD. (Inset) Top: solid curve is from an artificial movie created from a digitized action potential at 1 msec frame interval. Middle: samples corresponding to 16 msec frame interval. Bottom: linearly interpolated 16 msec samples superimposed on the upper action potential. Both the computer model (A) and optical data (B) show that APD error increases as frame interval increases for 50, 70, and 90% cutoff levels. APD error is the difference between the high-resolution and low-resolution action potentials (e.g., traces at bottom of inset).**

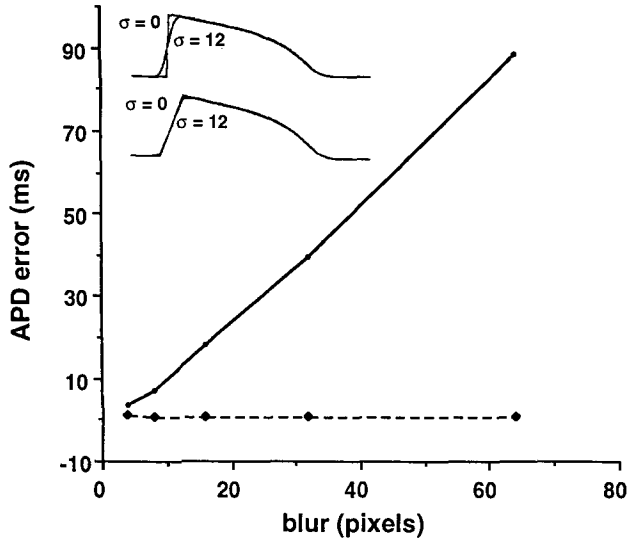


**FIGURE 9.** Computer model showing effect of the spatial filter on APD. APD error from the square wave movie data with different amounts of blur and subsequent filtering ( $\sigma = 2.5$ ). Error is defined as the difference between the blurred, filtered movies and the unblurred, unfiltered movie. Solid line: total APD error from both blur and filter. Dotted line: error from the filter. All APDs at the 90% level. (Inset) Top: time series of an action potential that reaches maximum value in 1 frame, superimposed over the same movie data after spatial filtering ( $\sigma = 12$ ). The spatial filter turns the step edge into a sinusoid. (Inset) Bottom: same data (with and without filtering) with a blur of 18 pixels. The effect of the filter is dramatically reduced.

filter size increases APD error and (b) increasing blur decreases the filter-induced error. Movies of the standard wave were blurred at different frame intervals, then filtered with a spatial filter with  $\sigma = 2.5$ . Figure 9 shows the total APD error from both blurring and filtering (solid line) and the APD error from filtering alone (dotted line) after subtracting the blurring error. Only at the smallest level of blur (4 pixels) is there any filter-induced APD error (~1 msec). Data are shown for the 90% cutoff level to exaggerate the error; filter-induced APD error was even less at the 50 and 70% levels. Although the spatial filter can affect APD, we conclude that, for the range of blur and filter sizes used for our data, the effects of the spatial filter on APD are negligible.

Varying amounts of amplitude noise were added to the standard movie; APD was calculated at every point in the image. For the standard movie the APD maps at 50, 70, and 90% levels were uniform over the entire image and equal to APDs measured from the time series by hand. Noise added to the movie increased the APD error (the difference between APDs in the noiseless and the noisy movies). Although the average APD of the map computed by the algorithm remained correct, the SD of the values increased as the level of noise increased (Fig. 10, upper plot). Spatial filtering ( $\sigma = 2.5$ ) of noisy movies significantly reduced the SD of APD error (Fig. 10, lower plot).

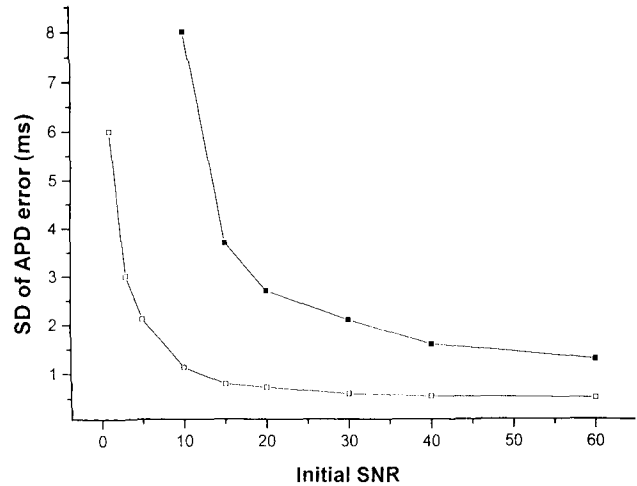


**FIGURE 10.** Computer model showing effect of noise on APD. Upper plot: Gaussian noise with varying SD was added to artificial movies of digitized action potentials. Decreasing SNR increased the uncertainty by increasing SD of APD differences, although the average APD value was the same as the noise-free movie. Lower plot: spatially filtering ( $\sigma = 2.5$ ) the same movies decreased the APD error. Initial SNR refers to SNR before filtering (*i.e.*, upper plot).

Discretizing the amplitude to a small number of levels has severe effects on the shape of the waveform over time. The inset of Fig. 11 shows an action potential quantized to 3 amplitude levels. For a given number of quantization levels, there were many different AP profiles, because all action potentials within a range of maximum voltages are mapped to the same amplitude level. As shown in Fig. 11, when the number of quantization levels was decreased, the SD of the APD error increased, although the average value was zero error. Here again, the spatial filter helps: by averaging neighborhood values, it reduces the SD of APD error.

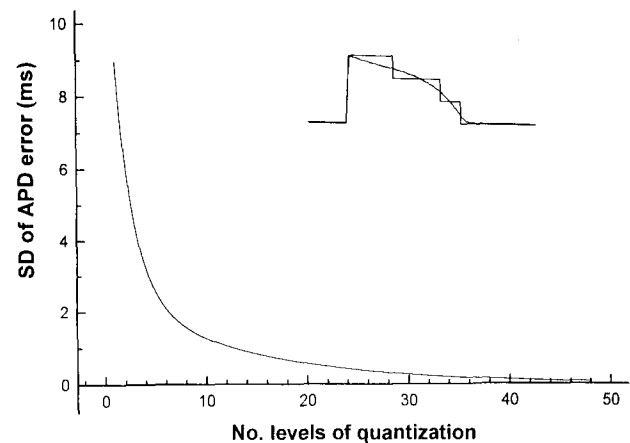


**FIGURE 11.** Computer model showing effect of amplitude quantization on APD. Using fewer levels to represent the action potential increased the SD of the measured APDs. (Inset) Digitized action potential superimposed over the same trace represented by 3 quantization levels.

## DISCUSSION

### *Summary*

CCDs collect and integrate incident photons over the frame interval, as opposed to sampling the signal. As a result, moving objects are blurred. Blur is proportional to magnification and the object's velocity, and inversely proportional to the frame rate of the system. For ideal input (*e.g.*, a moving step edge), the wave front may be localized with accuracy equal to the spatial resolution of the system. We have implemented a CCD optical mapping system capable of 60 to 240 Hz frame rates (16.7 to 4.2 msec frame intervals). We also developed a computer model of temporal integration in the CCD to study the effects of frame rate, quantization, noise and filtering on video movies of propagating waves.

Propagating waves were readily visualized in the video optical data, with SNRs between 1.5 and 4.4. A spatial filter that increased the SNR to 10 usually provided adequate action potentials for generating isochrone lines and APD measurements. The SNRs decreased as magnification or frame rate increased.

The video optical mapping system proved quite capable of generating accurate isochrone maps and determining CV. The computer model showed that, individually, blur, filtering, and quantization did not affect the ability to localize wave fronts. Noise did increase the uncertainty of measurements, but this was greatly reduced by application of the spatial filter. In the optical data from experiments, isochrone lines could be reliably assigned to wave fronts. Video optical measures of CV were as reliable as those done with a pair of microelectrodes, while additionally revealing complex patterns of activation.

The computer model identified numerous problems in accurately assessing APD in a system with low frame rates and low SNR. In the model, reducing the frame rate introduced a systematic error in APD in that cutoff levels at or  $>50\%$  resulted in incorrectly increased APDs. The blurring induced by the spatial filter introduced a similar systematic error, but this effect was negligible when it was superimposed on the blurring induced by a low frame rate. Increasing noise or decreasing the number of discrete levels representing the signal amplitude increased the scatter and uncertainty of APD values. In experimentally obtained data, optical action potentials displayed the same systematic error in APD from slow frame rates when compared with microelectrode recordings.

CV may be accurately determined, because video optical mapping can distinguish and localize individual wave fronts, but the slow frame rates of the present system are unable to represent faithfully the details of the action potential. To capture temporal details of the action potential, the sampling rate must be fast enough to represent the highest frequency components. Analysis of the power

spectra of digitized microelectrode recordings by Girouard *et al.* (13) determined that at least a 300 Hz sampling rate was necessary to reconstruct accurately the guinea pig ventricular action potential. Most of the action potential consists of the low-frequency repolarizing tail, which can be adequately sampled even with a 60 Hz system. Optical analysis of the high-frequency upstroke has typically been conducted with sampling rates from 10 to 100 kHz (11,25).

Although determination of accurate APDs from the optical video data is problematic, useful information may still be obtained. In many cases, the difference between optical and electrode APDs was 10 msec or less. APD error may be minimized by (a) faster frame rates, (b) lower magnification, (c) more quantization levels, (d) higher SNR, and (e) using the 50% repolarization level. A roving microelectrode may be used as a reference to determine the APD error for a given trial series. Relative differences in APD are evident: APD maps show gradients in APD over the entire area of tissue in view.

### *A Comparison of Techniques*

Optical monitoring with potentiometric dyes provides an alternative to standard electrophysiological techniques with many advantages (see Ref. 6 for a review). Multisite optical imaging systems fall roughly into three categories: photodiode arrays (PDAs), scientific CCD cameras, and video CCDs. Both propagation velocity and APD may be very accurately measured in optical mapping systems. Using a high precision photodiode system, Fast and Kléber (11) determined activation times with SD error of 30 msec, compared with micropipette recordings. Using a PDA, Efimov *et al.* (9) studied repolarization in whole guinea pig hearts. Their measurements of refractory periods were valid within 5 msec. Our own video system measured CV with an accuracy that was not significantly different from simultaneous electrode recordings, although it displayed a systematic error in APD measurement that ranged from 5 to 30 msec. Compared with video CCDs, PDAs (9,11,25) have many excellent features: higher SNRs (often  $>50$ ), larger dynamic range (12 or 16 bits), and faster acquisition rates (1 to 100 kHz). However, the number of elements in PDAs ranges from 3 to several hundred (10), with the largest just having just over 1,000 elements (16). The large number of sensor elements in CCD arrays ( $10^4$  to  $10^6$ ) permits recordings with high spatial resolution over a large area—ideal for analyzing complex wave patterns over several square centimeters. Activation of the tissue is visible on the monitor in real time, the field of view may be directed to the area of interest, and the magnification and frame rate may be quickly adjusted. The direct view of the tissue greatly simplifies problems of focusing and adjusting light levels. Because the recordings are themselves

pictures of the tissue, video imaging also provides a direct correlation of electrical patterns of activity with the gross anatomy of the preparation. It should also be noted that the CCD system excels at monitoring regions of slow conduction and block, which are precisely the areas of interest in many studies of arrhythmias (8), but are also those areas where extracellular electrograms are most difficult to interpret. The type of preparation and phenomena of interest will dictate the best recording system: PDAs with high temporal and low spatial resolution, or CCDs with low temporal and high spatial resolution.

Scientific CCDs (17) occupy a middle ground between PDAs and video CCDs. Their SNRs and dynamic range approach those of PDAs, while having a large number of recording elements. Their data readout is quite slow, however. Scientific cameras are typically used in low light circumstances with long accumulation times. They lack a separate storage array for frame transfer; thus, a shutter must be provided to prevent light from reaching the array during readout to avoid smearing. Because data are read off the chip at a fixed rate, readout rates may be increased by decreasing the number of pixels used (19). To achieve frame rates useful for studying arrhythmias, this means reducing the number of elements to a few hundred at most, in which case the camera resembles a PDA. The future will hopefully see cameras with the sensitivity of scientific-grade CCDs and even higher frame rates than the current video standard. The issues of blur and temporal resolution of moving objects discussed in this paper will continue to be relevant at the faster frame rates, because they are due to the integrating nature of CCD sensors. In summary, PDAs have high SNRs, dynamic range, and temporal resolution, but relatively few pixels. Scientific CCDs also possess good SNRs and dynamic range while additionally having many pixels, but they have extremely slow rates of frame readout. Standard RS-170 CCD cameras, although having low SNR and only 8-bit dynamic range, have large numbers of pixels and frame rates that are fast enough for the analysis of cardiac action potentials.

### CONCLUSIONS

CCD optical mapping is an excellent tool for studying CV and patterns of propagation in cardiac tissue. It has been used to study spiral wave reentry (5,23), rate-dependent conduction block (1), and wave front curvature (3) in thin slices of cardiac tissue, as well as arrhythmic activity in the whole rabbit heart (14). In this paper, we describe the CCD optical mapping system itself to provide a better understanding of its strengths and limitations. Optical mapping of transmembrane electrical activity in cardiac tissue using a CCD video camera is a reliable technique for the study of CV and patterns of propagation in

two dimensions. Measures of APD must be interpreted with the caveat that there are systematic errors resulting from slow frame rates. CCD mapping additionally permits direct correlation between electrical activity and the gross anatomy of the preparation. The CCD system described here uses a video rate camera capable of detecting action potentials in cardiac tissue in a single pass at 4.1 msec resolution—a necessity for tracking the nonrepetitive events of cardiac arrhythmias.

### REFERENCES

1. Baxter, W. T., J. M. Davidenko, C. Cabo, and J. Jalife. Video imaging of cardiac transmembrane activity. *SPIE Proc. Clin. Appl. Modern Imaging Technol.* 2132:357–366, 1994.
2. Blasel, G. G., and G. Salama. Voltage-sensitive dyes reveal a modular organization in monkey striate cortex. *Nature* 321:579–585, 1986.
3. Cabo, C., A. M. Pertsov, W. T. Baxter, J. M. Davidenko, R. A. Gray, and J. Jalife. Wave-front curvature as a cause of slow conduction and block in isolated cardiac muscle. *Circ. Res.* 75:1014–1028, 1994.
4. Cohen, L. B., B. M. Salzberg, H. V. Davila, W. N. Ross, D. Landowne, A. S. Waggoner, and C. H. Wang. Changes in axon fluorescence during activity: molecular probes of membrane potential. *J. Membr. Biol.* 19:1–36, 1974.
5. Davidenko, J. M., A. V. Pertsov, R. Salomonsz, W. Baxter, and J. Jalife. Stationary and drifting spiral waves of excitation in isolated cardiac muscle. *Nature* 355:349–351, 1992.
6. Dillon, S. M. Use of voltage sensitive dyes to record, map and image cardiac electrical activation. In: *Imaging analysis and simulation of the cardiac system*, edited by S. Sideman and R. Beyar. London: Freund Publishing, 1990, pp. 739–766.
7. Dillon, S., and M. Morad. A new laser scanning system for measuring action potential propagation in the heart. *Science* 214:453–456, 1981.
8. Dillon, S. M., M. A. Alessie, P. C. Ursell, and A. L. Wit. Influence of anisotropic tissue on reentrant circuit in the epicardial border zone of subacute canine infarcts. *Circ. Res.* 63:182–206, 1988.
9. Efimov, I. R., D. T. Huang, J. M. Rendt, and G. Salama. Optical mapping of repolarization and refractoriness from intact hearts. *Circulation* 90:1469–1480, 1994.
10. Falk, C. X., J. Y. Wu, L. B. Cohen, and A. K. Tang. Non-uniform expression of habituation in the activity of distinct classes of neurons in the *Aplysia* abdominal ganglion. *J. Neurosci.* 13:4072–4081, 1993.
11. Fast, V. G., and A. G. Kléber. Microscopic conduction in cultured strands of neonatal rat heart cells measured with voltage-sensitive dyes. *Circ. Res.* 73:914–925, 1993.
12. Frazier, D. W., P. D. Wolf, J. M. Wharton, A. S. L. Tang, W. M. Smith, and R. E. Ideker. Stimulus-induced critical point: mechanism for initiation of reentry in normal canine myocardium. *J. Clin. Invest.* 83:1039–1052, 1989.
13. Girouard, S. D., K. R. Laurita, and D. S. Rosenbaum. Unique characteristics of optically recorded action potentials. *J. Cardiovasc. Electrophysiol.* 7:1024–1038, 1996.
14. Gray, R. A., J. Jalife, A. Panfilov, W. T. Baxter, C. Cabo, J.

- Davidenko, and A. M. Pertsov. Nonstationary vortexlike reentrant activity as a mechanism of polymorphic ventricular tachycardia in the isolated rabbit heart. *Circulation* 91:2454–2469, 1995.
15. Grinvald, A. Real-time optical mapping of neuronal activity: from single growth cones to the intact mammalian brain. *Ann. Rev. Neurosci.* 8:263–305, 1985.
  16. Hirota, A., K. Sato, Y. Momose-Sato, T. Sakai, and K. Kamino. A new simultaneous 1020-site optical recording system for monitoring neural activity using voltage-sensitive dyes. *J. Neurosci. Methods* 56:187–194, 1995.
  17. Janesick, J. R., T. Elliott, S. Collins, M. M. Blouke, and J. Freeman. Scientific charge-coupled devices. *Opt. Eng.* 26:692–714, 1987.
  18. Kauer, J. S. Real-time imaging of evoked activity in local circuits of the salamander olfactory bulb. *Nature* 331:166–168, 1988.
  19. Lasser-Ross, N., H. Miyakawa, V. Lev-Ram, S. R. Young, and W. N. Ross. High time resolution fluorescence imaging with a CCD camera. *J. Neurosci. Methods* 36:253–261, 1991.
  20. Liu, Y., C. Cabo, R. Salomonsz, M. Delmar, J. Davidenko, and J. Jalife. Effects of diacetyl monoxime on the electrical properties of sheep and guinea pig ventricular muscle. *Cardiovasc. Res.* 27:1991–1997, 1993.
  21. Loew, L. M., L. B. Cohen, J. Dix, E. N. Fluhler, V. Montana, G. Salama, and J. Y. Wu. A naphthyl analog of the aminostyryl pyridinium class of potentiometric membrane dyes shows consistent sensitivity in a variety of tissue, cell, and model membrane preparations. *J. Membr. Biol.* 130:1–10, 1992.
  22. MacKay, C. D. Fast optical imaging techniques. In: *Fluorescence spectroscopy*, edited by O. S. Wolfbeis. New York: Springer-Verlag, 1993, pp. 25–30.
  23. Pertsov, A. M., J. M. Davidenko, R. Salomonsz, W. T. Baxter, and J. Jalife. Spiral waves of excitation underlie reentrant activity in isolated cardiac muscle. *Circ. Res.* 72:631–650, 1993.
  24. Ratzlaff, E. H., and A. Grinvald. A tandem-lens epifluorescence microscope: hundred-fold brightness advantage for wide-field imaging. *J. Neurosci. Methods* 36:127–137, 1991.
  25. Rohr, S., and B. M. Salzberg. Multiple site optical recording of transmembrane voltage (MSORTV) in patterned growth heart cell cultures: assessing electrical behavior, with microsecond resolution, on a cellular and subcellular scale. *Biophys. J.* 67:1301–1315, 1994.
  26. Russ, J. C. *The Image Processing Handbook*, Boca Raton, FL: CRC Press, 1992, pp. 1–445.
  27. Salama, G. Optical measurements of transmembrane potential in heart. In: *Spectroscopic membrane probes*, vol. 3, edited by L. M. Loew. Boca Raton, FL: CRC Press, 1988, pp. 137–199.
  28. Salama, G., and M. Morad. Merocyanine 540 as an optical probe of transmembrane electrical activity in the heart. *Science* 191:485–487, 1976.